Optical coherenscopy based on phase-space tomography

Alejandro Cámara, José A. Rodrigo, and Tatiana Alieva*

Universidad Complutense de Madrid, Facultad de Ciencias Físicas, Ciudad Universitaria s/n, Madrid 28040, Spain

*talieva@fis.ucm.es

Abstract: Partially coherent light provides attractive benefits in imaging, beam shaping, free-space communications, random medium monitoring, among other applications. However, the experimental characterization of the spatial coherence is a difficult problem involving second-order statistics represented by four-dimensional functions that cannot be directly measured and analyzed. In addition, real-world applications usually require quantitative characterization of the local spatial coherence of a beam in the absence of *a priori* information, together with fast acquisition and processing of the experimental data. Here we propose and experimentally demonstrate a technique that solves this problem. It comprises an optical setup developed for automatized video-rate measurement and a method –phase-space tomographic *coherenscopy*– allowing parallel data acquisition, processing, and analysis. This technique significantly simplifies the spatial coherence analysis and opens up new perspectives for the development of tools exploiting the degrees of freedom hidden into light coherence.

OCIS codes: (030.0030) Coherence and statistical optics; (070.2575) Fractional Fourier transforms; (140.3295) Laser beam characterization; (100.5070) Phase retrieval; (090.1995) Digital holography.

References

1. J. W. Goodman, *Statistical Optics* (Wiley-Interscience, 2000).
2. M. Born and E. Wolf, *Principles of Optics* (Cambridge University Press, 2006).
3. G. Gbur and T. D. Visser, "The structure of partially coherent fields," in *Progress in Optics* (Elsevier, 2010), **55**, 285–341.
4. A. A. Michelson and F. G. Pease, "Measurement of the diameter of Alpha-Orionis by the interferometer," Astrophys. J. **53**, 249–259 (1921).
5. Y. Cai and S.-Y. Zhu, "Ghost imaging with incoherent and partially coherent light radiation," Phys. Rev. E **71**, 056607 (2005).
6. B. I. Erkmen and J. H. Shapiro, "Ghost imaging: from quantum to classical to computational," Adv. Opt. Photon. **2**, 405–450 (2010).
7. F. Dubois, L. Joannes, and J.-C. Legros, "Improved three-dimensional imaging with a digital holography microscope with a source of partial spatial coherence," Appl. Opt. **38**, 7085–7094 (1999).
8. P. Kolman and R. Chmelík, "Coherence-controlled holographic microscope," Opt. Express **18**, 21990–22003 (2010).
9. X. Ma and G. R. Arce, "PSM design for inverse lithography with partially coherent illumination," Opt. Express **16**, 20126–20141 (2008).
10. X. Ma and G. Arce, *Computational Lithography*, Wiley Series in Pure and Applied Optics (Wiley, 2011).
11. T. Shirai, A. Dogariu, and E. Wolf, "Mode analysis of spreading of partially coherent beams propagating through atmospheric turbulence," J. Opt. Soc. Am. A **20**, 1094–1102 (2003).
12. P. Michel, C. Labaune, H. C. Bandulet, K. Lewis, S. Depierreux, S. Hulin, G. Bonnaud, V. T. Tikhonchuk, S. Weber, G. Riazuelo, H. A. Baldis, and A. Michard, "Strong reduction of the degree of spatial coherence of a laser beam propagating through a preformed plasma," Phys. Rev. Lett. **92**, 175001 (2004).

#188994 - $15.00 USD Received 17 Apr 2013; accepted 16 May 2013; published 22 May 2013

13. J. Wang, J.-Y. Yang, I. M. Fazal, N. Ahmed, Y. Yan, H. Huang, Y. Ren, Y. Yue, S. Dolinar, M. Tur, and A. E. Willner, "Terabit free-space data transmission employing orbital angular momentum multiplexing," Nature Photon. **6**, 488–496 (2012).
14. Z. Zalevsky, D. Medlovic, and H. M. Ozaktas, "Energetic efficient synthesis of general mutual intensity distribution," J. Opt. A **2**, 83–87 (2000).
15. M. J. Bastiaans, "The Wigner distribution function of partially coherent light," Opt. Acta **28**, 1215–1224 (1981).
16. M. Alonso, "Wigner functions in optics: describing beams as ray bundles and pulses as particle ensembles," Adv. Opt. Photon. **3**, 272–365 (2011).
17. G. S. Agarwal and R. Simon, "Reconstruction of the Wigner transform of a rotationally symmetric two-dimensional beam from the Wigner transform of the beam's one-dimensional sample," Opt. Lett. **17** [17], 1379–1381.
18. T. Alieva and F. Agullo-Lopez, "Reconstruction of the optical correlation function in a quadratic refractive index medium," Opt. Commun. **114**, 161–169 (1995).
19. C. Q. Tran and K. A. Nugent, "Recovering the complete coherence function of a generalized Schell model field," Opt. Lett. **31**, 3226–3227 (2006).
20. T. E. Gureyev, A. Roberts, and K. A. Nugent, "Partially coherent fields, the transport-of-intensity equation, and phase uniqueness," J. Opt. Soc. Am. A **12**, 1942–1946 (1995).
21. A. Cámara, T. Alieva, J. A. Rodrigo, and M. L. Calvo, "Phase space tomography reconstruction of the Wigner distribution for optical beams separable in Cartesian coordinates," J. Opt. Soc. Am. A **26**, 1301–1306 (2009).
22. K. A. Nugent, "Partially coherent diffraction patterns and coherence measurement," J. Opt. Soc. Am. A **8**, 1574–1579 (1991).
23. M. Santarsiero and R. Borghi, "Measuring spatial coherence by using a reversed-wavefront Young interferometer," Opt. Lett. **31**, 861–863 (2006).
24. A. I. González and Y. Mejía, "Nonredundant array of apertures to measure the spatial coherence in two dimensions with only one interferogram," J. Opt. Soc. Am. A **28**, 1107–1113 (2011).
25. L. Waller, G. Situ, and J. W. Fleischer, "Phase-space measurement and coherence synthesis of optical beams," Nature Photon. **6**, 474–479 (2012).
26. M. G. Raymer, M. Beck, and D. F. McAlister, "Complex wave-field reconstruction using phase-space tomography," Phys. Rev. Lett. **72**, 1137–1140 (1994).
27. A. Cámara, T. Alieva, J. A. Rodrigo, and M. L. Calvo, "Tomographic reconstruction of the Wigner distribution of non-separable beams," in *PIERS Proceedings* (2010), 526–530.
28. D. Mendlovic, R. G. Dorsch, A. W. Lohmann, Z. Zalevsky, and C. Ferreira, "Optical illustration of a varied fractional Fourier-transform order and the Radon—Wigner display," Appl. Opt. **35**, 3925–3929 (1996).
29. Y. Zhang, B.-Y. Gu, B.-Z. Dong, and G.-Z. Yang, "Optical implementations of the Radon–Wigner display for one-dimensional signals," Opt. Lett. **23**, 1126–1128 (1998).
30. A. Cámara, T. Alieva, J. A. Rodrigo, and M. L. Calvo, "Phase-space tomography with a programmable Radon–Wigner display," Opt. Lett. **36**, 2441–2443 (2011).
31. J. Radon, "On the determination of functions from their integral values along certain manifolds," IEEE Trans. Med. Imag. **5**, 170–176 (1986).
32. J. A. Rodrigo, T. Alieva, and M. J. Bastiaans, *Optical and Digital Image Processing* (Wiley-VCH Verlag, 2011), chap. 12.
33. J. A. Rodrigo, T. Alieva, and M. L. Calvo, "Programmable two-dimensional optical fractional Fourier processor," Opt. Express **17**, 4976–4983 (2009).
34. J. A. Rodrigo, T. Alieva, A. Cámara, Ó. Martínez-Matos, P. Cheben, and M. L. Calvo, "Characterization of holographically generated beams via phase retrieval based on Wigner distribution projections," Opt. Express **19**, 6064–6077 (2011).
35. X. Liu and K. H. Brenner, "Reconstruction of two-dimensional complex amplitudes from intensity measurements," Opt. Commun. **225**, 19–30 (2003).
36. E. Wolf, "New theory of partial coherence in the space-frequency domain. Part I: spectra and cross spectra of steady-state sources," J. Opt. Soc. Am. **72**, 343–351 (1982).
37. F. Gori, M. Santarsiero, R. Borghi, and G. Guattari, "Intensity-based modal analysis of partially coherent beams with Hermite–Gaussian modes," Opt. Lett. **23**, 989–991 (1998).
38. E. Tervonen, J. Turunen, and A. T. Friberg, "Transverse laser-mode structure determination from spatial coherence measurements: Experimental results," Appl. Phys. B **49**, 409–414 (1989).
39. J. C. Ricklin and F. M. Davidson, "Atmospheric turbulence effects on a partially coherent Gaussian beam: implications for free-space laser communication," J. Opt. Soc. Am. A **19**, 1794–1802 (2002).
40. Y. Yuan, Y. Cai, J. Qu, H. T. Eyyuboğlu, Y. Baykal, and O. Korotkova, "M2-factor of coherent and partially coherent dark hollow beams propagating in turbulent atmosphere," Opt. Express **17**, 17344–17356 (2009).
41. "Adaptive optics kits, tabletop deformable mirrors and more," Nature Photon. **5**, 27–27 (2011).
42. M. Bastiaans, "Transport equations for the Wigner distribution function in an inhomogeneous and dispersive medium," Opt. Acta **26**, 1333–1344 (1979).
43. J. W. Goodman, *Introduction to Fourier Optics* (Roberts & Company, Colorado, USA, 2005).

#188994 - $15.00 USD Received 17 Apr 2013; accepted 16 May 2013; published 22 May 2013

44. H. M. Ozaktas, Z. Zalevsky, and M. A. Kutay, *The Fractional Fourier Transform with Applications in Optics and Signal Processing* (Wiley, 2001).

1. Introduction

Numerous instruments and techniques used in science and technology are based on light characterization. The analysis of light spectrum, polarization, intensity distribution, and coherence provides valuable information about the light source or the medium where it propagates. While the measurements of some characteristics are well established, the diagnosis of spatial coherence, which by analogy with spectroscopy and microscopy might be referred to as *coherenscopy*, is still a challenging task. Nevertheless, additional degrees of freedom provided by coherence are prominent for many applications [1–3]. A historical example illustrating the relevance of light statistics is found in astronomy where the star size was estimated from the measurement of the degree of coherence (DoC) [4]. Modern coherence-based techniques include ghost imaging [5, 6], coherence controlled microscopy [7, 8], lithography [9, 10], and characterization of atmospheric [11] and plasma [12] instabilities. Moreover, the use of partially coherent light increases the transmission capacity of free-space communications [13] and improves information encoding [14].

Further applications of partially coherent light require the development of efficient techniques for coherence characterization. This problem is rather difficult because even in the scalar quasi-monochromatic case a two-dimensional (2D) beam is described in paraxial approximation by a complex-valued function of four variables, $\Gamma(\mathbf{r}_1,\mathbf{r}_2) = \langle f^*(\mathbf{r}_1)\, f(\mathbf{r}_2)\rangle$, known as mutual intensity (MI) [1, 2]. Here $\mathbf{r} = [x,y]^t$ is a position vector at the plane perpendicular to the beam propagation direction, $f(\mathbf{r})$ is a stochastic complex field amplitude, and $\langle\cdot\rangle$ stands for ensemble averaging. The MI gauges the field correlation at the points $\mathbf{r}_1$ and $\mathbf{r}_2$ via DoC: $\gamma(\mathbf{r}_1,\mathbf{r}_2) = \Gamma(\mathbf{r}_1,\mathbf{r}_2)/\sqrt{\Gamma(\mathbf{r}_1,\mathbf{r}_1)\,\Gamma(\mathbf{r}_2,\mathbf{r}_2)}$. Note that only the values $\Gamma(\mathbf{r},\mathbf{r}) = \left\langle |f(\mathbf{r})|^2\right\rangle$, corresponding to the intensity distribution, can be directly measured.

Instead of the MI, its Fourier transform (FT) respect to the position difference $\mathbf{r}_1 - \mathbf{r}_2$, known as Wigner distribution (WD) [15, 16], can be used for beam description. The WD is a real 4D function but it may take negative values that also impedes its direct measurement.

In the last decades, various methods have been proposed for MI or WD reconstruction [17–26], yet none has demonstrated to be feasible for quantitative estimation of the coherence state in the absence of *a priori* information. Some methods assume certain hypothesis about field model [18–20], its symmetry [17, 21] or coherence homogeneity [22]. Others apply pinhole [23, 24] or slit masks [25] which alter the measurements and decrease the signal to noise ratio caused by significant power reduction of the analyzed field. The phase-space tomography method [26], consisting of the WD reconstruction from its projections associated with intensity distributions, avoids these problems. Nevertheless, it is not widely used for coherence analysis due to three principal reasons: the absence of a setup for rapid acquisition of the required WD projections, the complexity of data processing for WD and MI recovery, and the inherent difficulty of analyzing these resulting 4D functions [27]. Practical experimental setups applying this method have been developed only for the coherence study of 1D optical signals [28–30].

Here we present a simple technique for complete quantitative analysis of the beam spatial coherence. Our solution exploits the WD projection diversity providing crucial advantages in data acquisition, processing, and analysis. It is experimentally demonstrated on several examples.

#188994 - $15.00 USD Received 17 Apr 2013; accepted 16 May 2013; published 22 May 2013

2. Principle of the technique

The *tomographic* technique proposed by Radon [31] consists in the reconstruction of an object from its projections associated to different directions. While in the case of the 2D object there is a unique choice of the rotation axes to gather the required projections, refereed to as *projection set*, in the case of the tomographic exploration of a N-dimensional object there exist numerous projection sets that can be used for its recovery. The choice of the proper projection set significantly simplifies the reconstruction process and the analysis of the results. For example, in the reconstruction of the horizontal sections of 3D object the acquisition of the vertical projections is more appropriate, Fig. 1(a). To obtain the same sections using the horizontal projections [see Fig. 1(b)], a prior reconstruction of the entire 3D object is required.

In phase-space tomography of an optical beam, the object is the WD [15, 16, 26]:

$$W(\mathbf{r},\mathbf{k}) = \frac{1}{\lambda^2}\int \mathrm{d}\mathbf{r}'\Gamma\left(\mathbf{r}-\mathbf{r}'/2,\mathbf{r}+\mathbf{r}'/2\right)\exp\left(-\mathrm{i}\mathbf{k}^t\mathbf{r}'\right), \tag{1}$$

where $\lambda = 2\pi/|\mathbf{k}|$ is the wavelength and $\mathbf{k} = [k_x, k_y]^t$ is the spatial frequency vector. In this case two independent angles, α and β (both covering a $\pi-$interval) associated with the rotation in two orthogonal planes of the phase space are needed to obtain the 2D projections required for WD recovery. The WD rotation is achieved by beam propagation thought certain optical systems [32], see Appendix. As in the 3D case, there exists a high diversity of the projection sets suitable for the complete beam characterization. Not all of them, however, easily provide meaningful information about the beam coherence. Here we demonstrate that the projection set, hereinafter referred as $\{P^{\alpha,\beta}(\mathbf{r})\}$, obtained by rotating the WD on the yk_y and xy planes for angles α and β, respectively, is appropriate for this task. In this case, the interpretation of the 4D MI is significantly simplified by analyzing its 2D sections.

The projection set $\{P^{\alpha,\beta}(\mathbf{r})\}$ comprises several subsets, $\{P^{\alpha,\beta}(\mathbf{r})\}_{\beta_0}$, defined by fixing $\beta = \beta_0$, which are acquired consecutively. Each subset provides the information about field correlation at whichever points $\mathbf{r}_1$ and $\mathbf{r}_2$ that are contained in a line which forms an angle β_0 with axes y. The MI at such a line is defined as $\Gamma_{\beta_0}(\mathbf{r}_0,s) = \Gamma(\mathbf{r}_0,\mathbf{r}_0+s\mathbf{n})$, where $\mathbf{r}_0$ is the reference point, $\mathbf{n} = [-\sin\beta_0, \cos\beta_0]^t$ and s are the direction and running coordinate of the line, respectively. Analogously, the profiles of the DoC are defined as $\gamma_{\beta_0}(\mathbf{r}_0,s) = \gamma(\mathbf{r}_0,\mathbf{r}_0+s\mathbf{n})$.

In particular, the $\Gamma_0(\mathbf{r}_0,s)$ is recovered from the projection subset $\{P^{\alpha,\beta}(\mathbf{r})\}_{\beta_0=0}$, see the scheme depicted in Fig. 1(c). Indeed, it is sufficient for the tomographic reconstruction of the WDs, $W_{x_0}(y,k_y)$, of the 1D field $f(x_0,y)$ for any value of x_0. Specifically, from the $W_{x_0}(y,k_y)$ associated with the projection subset *slice* $\{P^{\alpha,\beta}(x_0,y)\}_0$, for a fixed x_0, the MI is recovered:

$$\Gamma_0(\mathbf{r}_0,s) = \frac{\lambda}{2\pi}\int \mathrm{d}k_y W_{x_0}(y_0+s/2,k_y)\exp(\mathrm{i}sk_y). \tag{2}$$

It provides the coherence relation between the field at a reference point $\mathbf{r}_0$ and any other points contained in the vertical line $x = x_0$ defining the 1D *profile* of the MI.

The information obtained from the projection subset $\{P^{\alpha,\beta}(\mathbf{r})\}_0$ can be analyzed in several ways. In particular, the amplitude and phase of $\Gamma_0(\mathbf{r}_0,s)$ and $\gamma_0(\mathbf{r}_0,s)$ can be represented as a 2D function of (y_0,s) or (x_0,s), as well as 1D profiles. Alternatively, the corresponding WDs providing phase-space representations can be studied. Therefore, this method offers a diversity of tools applicable for the analysis of light statistics depending on the standing problem.

To find the coherence relations for two points with different x coordinates, one has to perform the rotation in the xy plane for the corresponding angle β_0 and to repeat the procedure described above using the projection subset $\{P^{\alpha,\beta}(\mathbf{r})\}_{\beta_0}$. Doing this, we recover the desired information avoiding the reconstruction of the entire 4D WD and its posterior processing. The projection set

#188994 - $15.00 USD Received 17 Apr 2013; accepted 16 May 2013; published 22 May 2013

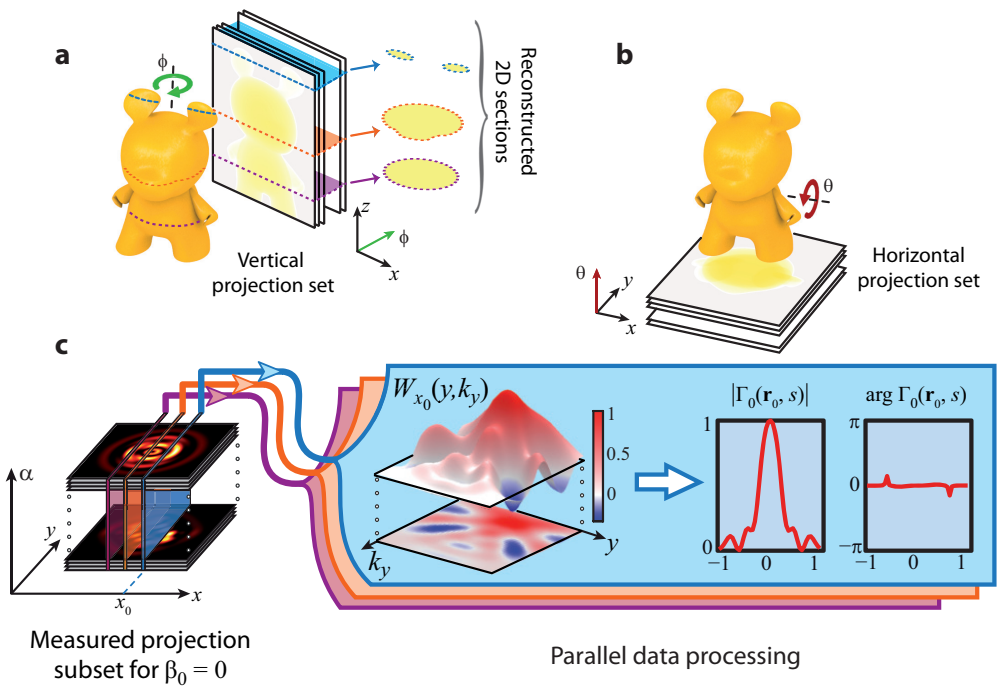

Fig. 1. Tomographic data acquisition and processing schemes. (a-b), Examples illustrating different projection choices available in conventional tomography of 3D objects. The vertical projection set drastically simplifies the reconstruction of the horizontal 2D sections of the 3D object. (c), Scheme of the proposed tomographic coherenscopy technique: the projection subset is measured for a fixed β_0 and then fed into the reconstruction algorithm providing parallel processing. The Wigner distribution $W_{x_0}(y,k_y)$ is reconstructed for each projection subset slice defined by both β_0 and x_0, for instance see the blue slice. From the $W_{x_0}(y,k_y)$, the corresponding amplitude and phase profiles of the MI are retrieved. This calculation is performed in parallel for the rest of the considered slices, for example the orange and purple ones.

$\{P^{\alpha,\beta}(\mathbf{r})\}$ has to be measured and processed for the complete beam characterization. Although the amount of data is the same as in other realizations of phase-space tomography, our technique brings powerful benefits compared to them:

1. The data acquisition and processing tasks are performed simultaneously since every projection subset is an independent entity. Moreover, as one projection subset slice is independent of the rest, the data processing is inherently prepared for parallel computing. These facts significantly speed up the reconstruction of the MI.

2. Physically meaningful information is obtained from a reduced number of projections. This allows starting the beam analysis before the complete projection set is acquired.

To implement this method, an efficient system for automatized acquisition of the required WD projection set is needed. The coherenscope setup sketched in Fig. 2(b), which is composed by two spatial light modulators (SLMs) and a CCD camera (see Methods), is well-suited for this task. It is based on the device developed in Ref. [33].

#188994 - $15.00 USD Received 17 Apr 2013; accepted 16 May 2013; published 22 May 2013

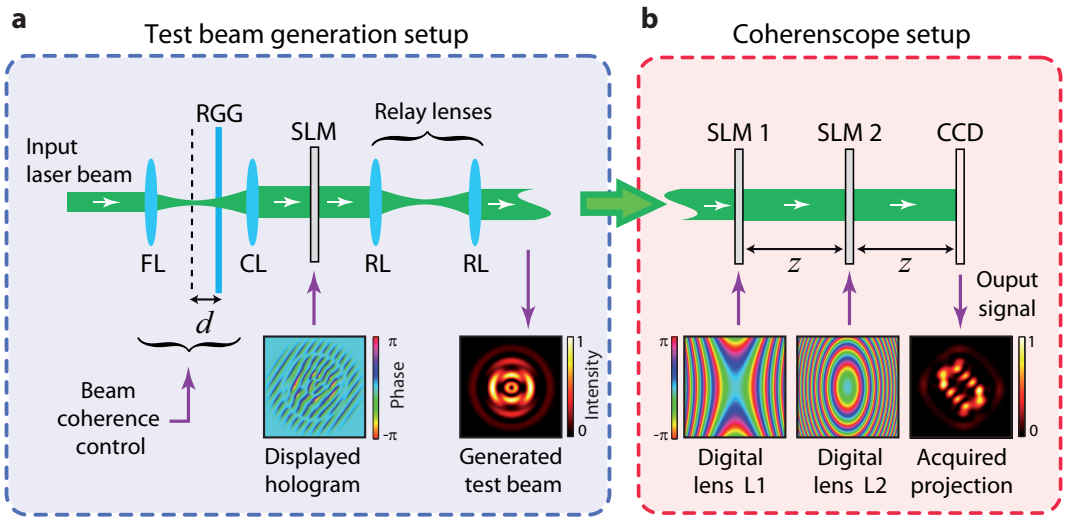

Fig. 2. Sketch of the experimental setups. (a), Setup for generation of test beams. While the degree of coherence of the test beam is controlled by the position d of the RGG diffuser, the spatial shaping of its amplitude and phase is achieved by a phase hologram addressed into the SLM. The diffuser is placed between the focusing (FL) and the collimating (CL) lenses. (b), Coherenscope setup. The test beam is projected by the relay lenses (RL) into the coherenscope setup which comprises two SLMs and a CCD camera placed at a fixed distance z. SLM 1 and SLM 2 address digital lenses to measure the required WD projections at video-rate, see Methods. As an example, the insets show the case of the WD projection acquisition corresponding to $\alpha = 5\pi/4$ and $\beta_0 = 0$.

3. Experimental results

The proposed technique is coherence-agnostic and does not require *a priory* information about the beam. To demonstrate its feasibility we consider several completely and partially coherent test beams synthesized by computer generated holograms (CGHs). The setup used for beam generation is sketched in Fig. 2(a). A CGH created following the approach reported in [34] is addressed into a SLM. Note that the rotating ground glass (RGG) diffuser is only used for the generation of partially coherent beams in the Experiment 2. The test beam is projected by the relay lenses into the input plane (SLM 1) of the coherenscope sketched in Fig. 2(b).

In the coherent case, Experiment 1, we compare the phase and amplitude distributions of the retrieved MI with the ones obtained applying an alternative method based on a well-established iterative algorithm. The characteristics recovered in Experiments 2 and 3 for partially coherent light, with homogeneous and non-homogeneous amplitude of DoC, are compared with the ones estimated using the coherence theory. Each measured projection subset contains 180 WD projections $P^{\alpha,\beta_0}(\mathbf{r})$ for $\alpha \in [\pi/2, 3\pi/2]$.

3.1. *Experiment 1: Coherent beam*

The coherent test beam is given by the superposition of two Laguerre-Gaussian modes $\mathrm{LG}_{p,l}(\mathbf{r})$: $\mathrm{LG}_{0,3}(\mathbf{r}) + \mathrm{LG}_{4,1}(\mathbf{r})$, where p and l are the radial and azimuthal indices, correspondingly. In order to prove the correct generation of the test beam, the measured distributions of its intensity, Fig. 3(a), and phase, Fig. 3(b), which completely describe a coherent beam, are compared with the theoretically predicted ones. The experimental phase distribution is determined using the iterative phase retrieval (IPR) technique developed in [34], which is based on

#188994 - $15.00 USD Received 17 Apr 2013; accepted 16 May 2013; published 22 May 2013

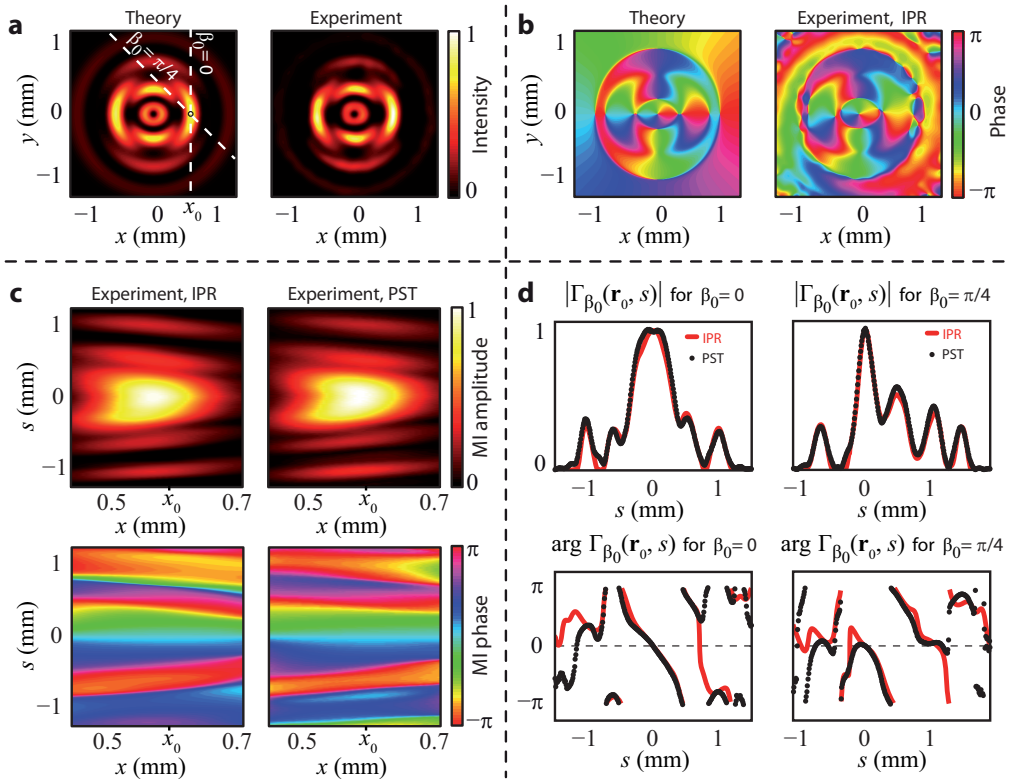

Fig. 3. Experiment 1: Analysis of the coherent beam. (a-b), Theoretical and experimentally obtained intensity and phase distributions of the input test beam $LG_{0,3}+LG_{4,1}$. The experimental phase is reconstructed via an iterative phase retrieval (IPR) algorithm. (c), Amplitude and phase of the reconstructed MI obtained via IPR and phase-space tomography (PST). (d), Amplitude and phase profiles of the MI, $\Gamma_{\beta_0}(\mathbf{r}_0, s)$, corresponding to $\beta_0=0$ and $\beta_0=\pi/4$, both sharing the reference point $\mathbf{r}_0=[0.6,0]^t$ mm as indicated in (a).

the Gerchberg-Saxton algorithm. The good agreement between these results demonstrates the high fidelity of the beam generation setup.

For a realistic analysis of the coherenscope performance, we compare the MI phase and amplitude recovered via phase-space tomography with the ones obtained via the IPR method, referred to as PST-MI and IPR-MI, respectively. In the reconstruction of PST-MI we have measured two projection subsets for angles $\beta_0=0$ and $\beta_0=\pi/4$. As an example, the WD projections for $\beta_0=0$ are shown in (Media 1) online (coherent case). The amplitude and phase maps of the reconstructed MI, $\Gamma_0(\mathbf{r}_0,s)$, for fixed y_0 and running x_0 and s, are displayed in Fig. 3(c) together with the corresponding maps for IRP-MI. Since the MI of the coherent beam is a product of the complex field amplitude, $\Gamma(\mathbf{r}_1,\mathbf{r}_2)=f(\mathbf{r}_1)\,f^*(\mathbf{r}_2)$, the phase of the field can be defined from the phase of the MI up to a constant factor. Note that the information obtained from the subset $\{P^{\alpha,\beta}(\mathbf{r})\}_0$ is not enough for this goal because the relative phase between any two vertical profiles is unknown. Fortunately, following the approach proposed in [35] this uncertainty is resolved if at least one MI phase profile along any non-vertical line ($\beta_0\neq 0$) is obtained.

The amplitude and phase profiles of both PST-MI and IPR-MI are displayed in Fig. 3(d). They are taken along the lines containing the point $\mathbf{r}_0=[0.6,0]^t$ mm, which form the angle $\beta_0=0$ and $\beta_0=\pi/4$ with the vertical axes, as indicated in Fig. 3(a). The good agreement be-

#188994 - $15.00 USD Received 17 Apr 2013; accepted 16 May 2013; published 22 May 2013

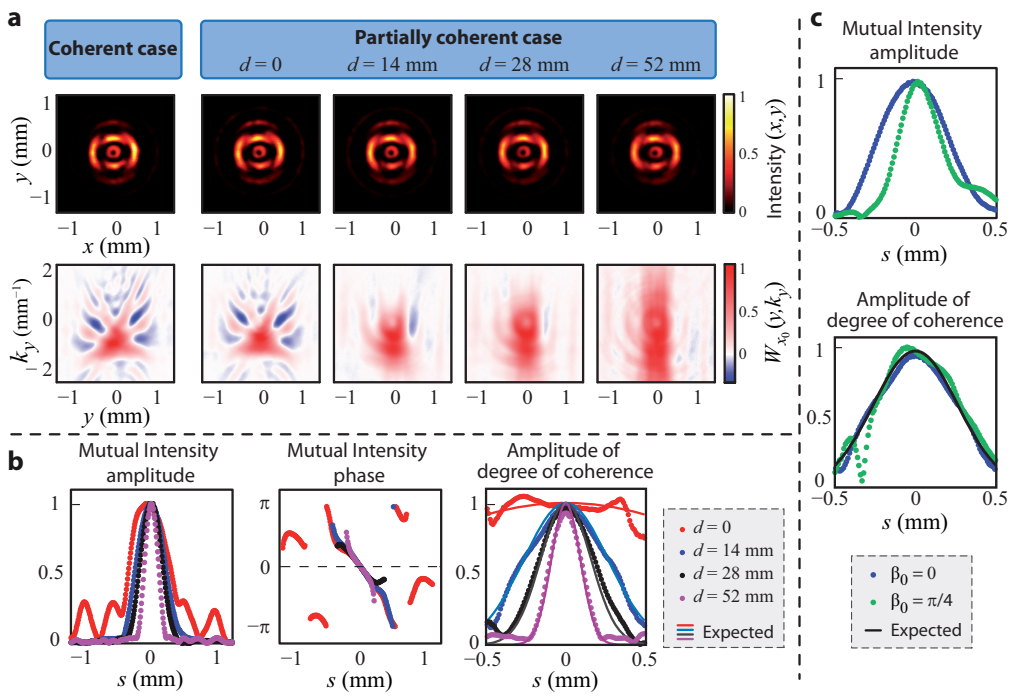

Fig. 4. Experiment 2: Analysis of beams with Gaussian-envelope amplitude of DoC. (a), Intensity distributions of the test beams with different degrees of coherence (first row). The WDs of the beams $W_{x_0}(y,k_y)$ for $x_0 = 0.6$ mm exhibit hidden differences associated with their coherence state (second row). (b), Amplitude and phase profiles of the MI and the DoC for the RGG positions $d = 0$, 14, 28, and 52 mm. These profiles correspond to $\Gamma_{\beta_0}(\mathbf{r}_0,s)$ and $\gamma_{\beta_0}(\mathbf{r}_0,s)$ for $\beta_0 = 0$ and $\mathbf{r}_0 = [0.6,0]^t$ mm. (c), Comparison between the profiles $|\Gamma_{\beta_0}(\mathbf{r}_0,s)|$ and $|\gamma_{\beta_0}(\mathbf{r}_0,s)|$ for $d = 14$ mm corresponding to $\beta_0 = 0$ and $\beta_0 = \pi/4$, sharing the same reference point $\mathbf{r}_0 = [0.6,0]^t$ mm. Solid curves: theoretically expected amplitudes of the DoC.

tween these results demonstrates the feasibility of our technique for characterization of coherent beams.

3.2. *Experiment 2: Beams with Gaussian-envelope amplitude of DoC*

The major strength of our technique is the analysis of partially coherent beams. The generation of beams with a homogeneous DoC amplitude is achieved by using a RGG diffuser and an SLM as sketched in Fig. 2(a). The diffuser transforms the spatially-coherent Gaussian laser beam into an incoherent Gaussian beam. The width of the latter depends on the distance d between the RGG diffuser and the Fourier plane of the focusing lens (FL), see Fig. 2(a). According to the Van Cittert-Zernike theorem [1, 2], the incoherent light emerging from the diffuser acquires a certain DoC after its propagation through the beam generation system. In particular, on the SLM plane, it is described by the MI function $\Gamma_d(\mathbf{r}_1,\mathbf{r}_2)$ corresponding to the Gaussian Schell model, see Appendix. The amplitude of the DoC is the Gaussian function $|\gamma_d(\mathbf{r}_1,\mathbf{r}_2)| = \exp\left[-\pi(\mathbf{r}_1-\mathbf{r}_2)^2/w_c^2\right]$, where w_c is inversely proportional to the width w of the beam illuminating the diffuser. Since w_c depends on d, it is possible to control the DoC of the generated beam by varying the diffuser position (d). This Gaussian Schell-model

beam is then modulated by the SLM that encodes the hologram used in the Experiment 1. Thus, the partially coherent test beam is described by $\Gamma(\mathbf{r}_1,\mathbf{r}_2) = \Gamma_d(\mathbf{r}_1,\mathbf{r}_2)\,\Gamma_c(\mathbf{r}_1,\mathbf{r}_2)$ where Γ_c is the same MI as in the coherent case. The amplitude of DoC of the resulting beam satisfies $|\gamma(\mathbf{r}_1,\mathbf{r}_2)| = |\gamma_d(\mathbf{r}_1,\mathbf{r}_2)|$ because $|\gamma_c(\mathbf{r}_1,\mathbf{r}_2)| = 1$. Moreover, $|\gamma_d(\mathbf{r}_1,\mathbf{r}_2)|$, and therefore $|\gamma(\mathbf{r}_1,\mathbf{r}_2)|$, are homogeneous functions since they depend only on the distance $r = |\mathbf{r}_1 - \mathbf{r}_2|$.

Four partially coherent beams have been generated for $d = 0$, 14, 28, and 52 mm, and the corresponding projection subsets $\{P^{\alpha,\beta}(\mathbf{r})\}_0$ have been acquired. In (Media 1) online, the experimental WD projection subsets associated with $d = 14$ and 52 mm and the coherent case are displayed. The 2D WD functions $W_{x_0}(y,k_y)$, where $x_0 = 0.6$ mm, are reconstructed for each beam, see Fig. 4(a). Although the intensity distributions of these beams are similar, the corresponding WDs exhibit significant differences. Specifically, the "spider-like" structure, with clearly distinguishable regions where the WD is negative, is gradually washed out as the DoC decreases. The largest distance $d = 52$ mm corresponds to the partially coherent beam with the lowest DoC, and the associated WD is almost independent of the spatial frequency coordinate, which is a typical behavior of incoherent light.

Analogously to the WD details, the side lobes of the MI amplitude profiles are washed out when the coherence decreases as shown in Fig. 4(b). We also observe that the phase profiles of the MI corresponding to $d = 0$ and 14 mm are similar where the MI amplitudes are above the noise level. Therefore, it is possible to recover the phase of $\Gamma_c(\mathbf{r}_1,\mathbf{r}_2)$ from which the information of the object modulating the beam (in our case the SLM) can be determined. This fact can be exploited for imaging of weakly absorbing specimens where the decrease of DoC results in speckle-noise reduction.

The experimental profiles of the DoC amplitude, which exhibit Gaussian form, are in good agreement with the theoretical model discussed in Appendix, see Fig. 4(b). The DoC amplitude of the beam is homogeneous and depends only on $s = |\mathbf{r}_1 - \mathbf{r}_2|$ while the amplitude of the MI is not. This is appreciated in Fig. 4(c), where the profiles of the $|\Gamma_{\beta_0}(\mathbf{r}_0,s)|$ and $|\gamma_{\beta_0}(\mathbf{r}_0,s)|$ are shown for the two crossed lines indicated in Fig. 3(a). As expected, the Gaussian curves of DoC amplitudes coincide except for the neighbourhood of the point $s = -0.33$ mm, where both the intensity and MI vanish for the profile corresponding to $\beta_0 = \pi/4$.

3.3. *Experiment 3: Beams with non-homogeneous amplitude of DoC*

Light with non-homogeneous amplitude of DoC is generated as incoherent composition of orthogonal modes $\psi_n(\mathbf{r})$ using the mode expansion approach [36–38]. In this case the MI is expressed as $\Gamma(\mathbf{r}_1,\mathbf{r}_2) = \sum_n a_n \psi_n(\mathbf{r}_1)\,\psi_n^*(\mathbf{r}_2)$, where a_n are real non-negative constants. In our experiment, two Laguerre-Gaussian modes, $\psi_1(\mathbf{r}) = \mathrm{LG}_{0,3}(\mathbf{r})$ and $\psi_2(\mathbf{r}) = \mathrm{LG}_{4,1}(\mathbf{r})$ whose intensity distributions are displayed in Fig. 5(a), have been used. Two partially coherent beams, refereed below as beam A and beam B, corresponding to the pair of constants $(a_1, a_2) = (0.5, 0.5)$ and $(a_1, a_2) = (0.25, 0.75)$, respectively, have been created by time multiplexing. Their intensity distributions are shown in Fig. 5(a).

In Fig. 5(b) we observe that the amplitude profiles of DoC, $\gamma_0(\mathbf{r}_1,s)$, for beams A (first row) and B (second row), where $\mathbf{r}_1 = [0.12, 0]^t$ mm, fit well with the theoretically predicted ones. Both beams are approximately coherent, $|\gamma_0(\mathbf{r}_1,s)| \approx 1$, for the interval around $s = 0$ where the mode $\psi_2(\mathbf{r})$ is dominant. In contrast, for the region $|s| > 0.3$ mm, where the contribution of both modes is similar, the DoC is less than 1. This decrease of the coherence is more clearly manifested for the beam A since both composing modes, ψ_1 and ψ_2, have equal weight.

The profiles $|\gamma_0(\mathbf{r}_1,s)|$ and $|\gamma_0(\mathbf{r}_2,s)|$ with $\mathbf{r}_2 = [0.35, 0]^t$ mm, see Fig. 5(c) (see second panel), demonstrate the non-homogeneity of the DoC amplitude present in the beam A. The field correlations for the reference point $\mathbf{r}_1$ can be explained easily from the analysis of the intensity distributions of the modes [see the first panel of Fig. 5(c)]. Since $\psi_1(x_1, 0) \approx 0$ the

#188994 - $15.00 USD Received 17 Apr 2013; accepted 16 May 2013; published 22 May 2013

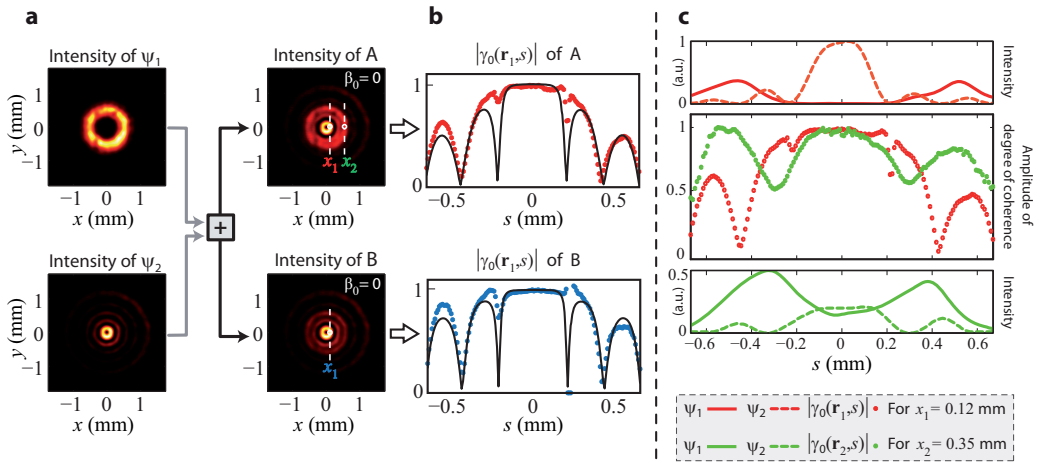

Fig. 5. Experiment 3: Analysis of beams with non-homogeneous amplitude of DoC. (a), Intensity distributions of the two modes $\psi_1(\mathbf{r})$ and $\psi_2(\mathbf{r})$ (first column) used for the generation of the partially coherent beams A and B (second column). (b), Comparison between the experimentally obtained (points) and numerically simulated (solid lines) profiles $|\gamma_0(\mathbf{r}_1,s)|$ with $\mathbf{r}_1 = [x_1,0]^t = [0.12,0]^t$ mm for the beams A and B. The profiles correspond to the white dashed lines drawn in (a) at the second column. (c), The profiles $|\gamma_0(\mathbf{r}_1,s)|$ and $|\gamma_0(\mathbf{r}_2,s)|$ for the beam A, with the previously defined $\mathbf{r}_1$ (second panel, red points) and $\mathbf{r}_2 = [x_2,0]^t = [0.35,0]^t$ mm (second panel, green points), demonstrate the non-homogeneity of the amplitude of DoC. The profile associated with the reference point $\mathbf{r}_2$ corresponds to the white dashed line drawn in (a). The first and third panels present the intensity of the modes $\psi_1(\mathbf{r})$ (solid line) and $\psi_2(\mathbf{r})$ (dashed line), which form the beam A, along the line associated with x_1 and x_2, correspondingly. They are used to help the interpretation of the DoC profiles.

coherence is governed by the mode $\psi_2(x_1,s)$ whose intensity distribution reaches a maximum value at $s=0$. As expected, the minima of $|\gamma_0(\mathbf{r}_1,s)|$ coincide with the points where intensity of the mode $\psi_2(x_1,s)$ vanishes and its maxima correspond to the local maxima of $|\psi_2(x_1,s)|^2$. On the other hand, the interpretation of the coherence curve $|\gamma_0(\mathbf{r}_2,s)|$ is not so straightforward because for the reference point $\mathbf{r}_2$ both modes have similar contributions [see the third panel of Fig. 5(c)]. In this case not only the relative intensity but also the phase distributions of the modes have to be taken into account for DoC estimation, which underlines the complexity of the beam coherence state. Nevertheless, it is successfully characterized using the coherenscope.

4. Discussion

The considered examples verify that the proposed technique is well-suited for quantitative and comprehensive study of completely and partially coherent optical fields, which makes it attractive for real-world applications. This technique offers diverse tools for beam analysis including MI, DoC, and WD. In contrast to other methods, it provides information, not only about the amplitudes of the MI and the DoC, but also about their phase. This fact paves the way to the application of partially coherent light for quantitative imaging of weakly absorbing specimens. The advantages of coherent and incoherent light, such as phase recovery of the diffracted field and speckle-noise reduction, can be combined by controlling the DoC of the involved light. On the other hand, the phase-space representation can be helpful for the design and characterization of optical systems, structurally stable beams, and spatially nonstationary fields [16].

#188994 - $15.00 USD Received 17 Apr 2013; accepted 16 May 2013; published 22 May 2013

The diagnosis of coherence is also important for random media monitoring and free-space communications. It has been reported [39,40] that partially coherent beams are less sensitive to distortions caused by the propagation in random media than their coherent counterparts, making them of interest for free-space laser communications and sensing. Another recently proposed scheme for data transmission employing orbital angular momentum multiplexing use, as in the Experiment 3, collinear incoherent mode combination for information encoding [13]. The effectiveness of the information transmission can be evaluated by the proposed coherenscopy technique.

The developed coherenscope setup comprises two programmable SLMs based on the liquid crystal technology. Other SLM devices such as deformable mirrors (DMs) [41] can be used to achieve faster measurement of the required WD projections. The rapid response of the DMs and sCMOS-based cameras can significantly reduce the data acquisition time to the range of few milliseconds. Moreover, efficient numerical algorithms for data processing implemented in a highly parallel processor (e.g. graphic processing units, GPU) lead to real-time coherence analysis. Independently from the considered SLM technology, the versatility of the coherenscope system makes it a promising tool for research and industrial applications.

In principle the proposed technique can be extended to the characterization of the coherence state of vector and band-limited beams by incorporation of polarization and spectroscopic elements.

5. Methods

5.1. Experimental setup for beam generation

The optical setup sketched in Fig. 2(a) allows generating several test beams with controlled DoC. A coherent test beam is analyzed in Experiment 1 while two different kinds of partially coherent beams are studied in Experiment 2 and 3. To control the DoC of the laser beam (wavelength of $\lambda = 532$ nm, and power of 50 mW), a RGG diffuser (Thorlabs DG20-120-MD, 120 grit polished) is used in Experiment 2. The diffuser rotating at 60 rpm is placed between two spherical convergent lenses operating in a 4-f configuration (i.e. Keplerian telescope) as depicted in Fig. 2(a). Both are NBK-7 glass lenses, where the first one works as a focusing lens (FL, focal length of 5 cm) and the second one acts as a collimation lens (CL, focal length of 25 cm). Four beams with different DoC obtained for the distance (between the back focal plane of FL and the diffuser) $d = 0$, 14, 28 and 52 mm, are generated. The light scattered from the diffuser illuminates a phase-only SLM (Holoeye PLUTO, 8-bit gray-level, pixel pitch of $8\,\mu$m, and 1920×1080 pixels) in which a computer generated phase hologram is displayed to shape the intensity and phase distributions of the test beam, as reported in Ref. [34]. In Experiment 1, the diffuser is removed from the setup to generate the coherent test beam. The generation of partially coherent beams given as incoherent superposition of Laguerre-Gaussian modes, Experiment 3, is performed by time multiplexing of holograms and therefore it does not require a RGG diffuser.

In our case, each test beam corresponds to an optical vortex given by a combination of Laguerre-Gaussian modes defined as

$$\mathrm{LG}_{p,l}\left(\mathbf{r};w\right) = A L_p^{|l|}\left(\frac{2\pi}{w^2}r^2\right)\exp\left(-\frac{\pi}{w^2}r^2\right)\exp\left(\mathrm{i}l\phi\right),$$

where $r^2 = x^2 + y^2$ and $\tan\phi = y/x$ are the polar coordinates, A is a normalization constant, w is the beam waist, and $L_p^{|l|}$ is the Laguerre polynomial with radial index p and azimuthal index l (i.e. topological charge). Specifically, the $\mathrm{LG}_{0,3}$ and $\mathrm{LG}_{4,1}$ modes were used as a base for the generation of both completely and partially coherent beams. The beam waist is expressed as

#188994 - $15.00 USD Received 17 Apr 2013; accepted 16 May 2013; published 22 May 2013

$w = \sqrt{2\lambda z}$, where $z = 50$ cm is the distance between the elements of the coherenscope setup sketched in Fig. 2(b).

Two identical relay lenses (RL, NBK-7 glass convergent lens with focal length of 25 cm), working as $1\times$ telescope, are used to project the test beam as an input signal into the coherenscope setup, see Fig. 2.

5.2. *Experimental coherenscope setup*

The coherenscope setup, Fig. 2(b), based on two phase-only SLMs (Holoeye LCR-2500, 8-bit gray-level, pixel pitch of $19\,\mu$m, and 1024×768 pixels) is used to obtain the WD projections of the generated test beam. These projections are acquired and stored as images using a CCD camera (Imaging Source DMK 41BF02, 8-bit gray-level, pixel size of $4.65\,\mu$m, and 1280×960 pixels). The distance between the SLMs and the CCD camera is fixed at $z = 50$ cm as sketched in Fig. 2(b). Each SLM displays a digital lens which varies as a function α and β in order to generate the required WD projection set $\{P^{\alpha,\beta}(\mathbf{r})\}$. The focal length of the digital lens is given as a function of the angle α, while β corresponds to the lens rotation angle. See Appendix for further details. Fig. 1(b) shows the phase maps of the digital lenses (SLM 1 and SLM 2) used to obtain the WD projection $P^{5\pi/4,0}(\mathbf{r})$ referred to as output signal. The whole process comprising setup control, projection acquisition, as well as data processing is achieved using a dedicated Matlab program developed by us.

Appendix

Phase-space tomography

The Wigner distribution is nowadays widely applied for beam description (see, for example, Refs. [15, 42] and the recent review [16] including the references cited therein). The WD is related to the MI through the Fourier transform (see Eq. (1) from the main text) which for experimental analysis is usually written in the form

$$W_f(\mathbf{r},\mathbf{p}) = \frac{1}{\sigma^2}\int \mathrm{d}\mathbf{r}'\,\Gamma\left(\mathbf{r}-\mathbf{r}'/2,\mathbf{r}+\mathbf{r}'/2\right)\exp\left(-\mathrm{i}2\pi\frac{\mathbf{p}^t\mathbf{r}'}{\sigma^2}\right), \tag{3}$$

where $\mathbf{p} = \sigma^2\mathbf{k}/2\pi = [u,v]^t$ is a vector, with the same units as $\mathbf{r}$, proportional to the spatial frequency vector $\mathbf{k}$ and σ is a scaling factor with units of length. The vectors $\mathbf{r}$ and $\mathbf{p}$ span the four dimensional phase space. Note that the use of the vector $\mathbf{p}$ instead of $\mathbf{k}$ also simplify the mathematical description of the phase-space tomography method. Similar variables are used in Fourier optics for the measurement and processing of the angular spectrum [43]. The parameter σ is usually defined by the optical system applied for the WD recovery.

Since the MI is a Hermitian function, the WD is real. However, it is not necessary positive, which impedes its direct measurement. Fortunately, the projections of the WD always take non-negative values and can be registered experimentally. The reconstruction method of the WD from its projections is regarded as phase-space tomography.

Phase-space tomography is based on the rotation of the WD of the beam after its propagation through certain optical systems. The WD, $W_{f^{\mathbf{T}}}(\mathbf{r},\mathbf{p})$, of the beam at the output plane of a first-order system described by the 4×4 symplectic ray transformation matrix $\mathbf{T} = [\mathbf{A},\mathbf{B};\mathbf{C},\mathbf{D}]$, is related to the WD at the input plane, $W_f(\mathbf{r},\mathbf{p})$, by an affine transformation [42]

$$W_{f^{\mathbf{T}}}(\mathbf{r},\mathbf{p}) = W_f\left(\mathbf{D}^t\mathbf{r}-\mathbf{B}^t\mathbf{p},-\mathbf{C}^t\mathbf{r}+\mathbf{A}^t\mathbf{p}\right), \tag{4}$$

which, in general, includes rotation, shearing and scaling in phase space. In particular, the rotations in phase space, which are described by the ray transformation matrix with parameters

$\mathbf{A} = \mathbf{D}$ and $\mathbf{B} = -\mathbf{C}$, are needed to apply the WD reconstruction method. The intensity distribution at the output plane of a phase space rotation system corresponds to the WD projection given by

$$\frac{1}{\sigma^2}\int \mathrm{d}\mathbf{p}\, W_{f^{\mathbf{T}}}(\mathbf{r},\mathbf{p}) = \left\langle \left| f^{\mathbf{T}}(\mathbf{r}) \right|^2 \right\rangle = P^{\mathbf{T}}(\mathbf{r}). \tag{5}$$

Measuring a proper projection set $\left\{P^{\mathbf{T}}(\mathbf{r})\right\}$ and using the inverse Radon transform, or other tomography reconstruction algorithm, the WD, and therefore the MI, can be recovered.

Four independent free parameters defining a phase-space rotation matrix provide a diversity of the projection sets suitable for the WD reconstruction. In Ref. [26] the tomographic method has been established for the projection set corresponding to the WD rotation on the planes xu and yv for angles $\alpha_{x,y}$, each one covering a π-interval. The optical system required for the acquisition of the corresponding projections $\left\{P^{\alpha_x,\alpha_y}_{FRFT}(\mathbf{r})\right\}$ is described by the two-dimensional separable fractional Fourier transform (FRFT) [44] associated with the matrix $\mathbf{T}_{FRFT}(\alpha_x,\alpha_y)$ defined by

$$\mathbf{A}_{FRFT} = \begin{bmatrix} \cos\alpha_x & 0 \\ 0 & \cos\alpha_y \end{bmatrix} \text{ and } \mathbf{B}_{FRFT} = \begin{bmatrix} \sin\alpha_x & 0 \\ 0 & \sin\alpha_y \end{bmatrix}. \tag{6}$$

Our choice for the projection set $\left\{P^{\alpha,\beta}(\mathbf{r})\right\}$ is related to the WD rotation on the planes yv and xy (and simultaneously uv) for angles α and β, respectively, covering a π-interval independently. The ray transformation matrix describing the required optical system is given by

$$\mathbf{A} = \begin{bmatrix} \cos\beta & -\sin\beta \\ \cos\alpha\sin\beta & \cos\alpha\cos\beta \end{bmatrix} \text{ and } \mathbf{B} = \begin{bmatrix} \cos\beta & -\sin\beta \\ \sin\alpha\sin\beta & \sin\alpha\cos\beta \end{bmatrix}. \tag{7}$$

Both projections sets can be automatically acquired using the programmable optical setup developed by us in Ref. [33]. The advantages of the last projection set are described in the main text of the article. Applying the inverse Radon transform to the projections corresponding to $\beta =$ constant, the WDs of the optical signals along lines parallel to the direction $\mathbf{n} = [-\sin\beta, \cos\beta]^t$ are obtained. The transformation of the corresponding WDs, according to equation (2) of the main text, yields the recovery of the MI of the field along the same lines.

Coherenscope setup

As previously mentioned, the proposed coherenscope setup is based on the fractional FT system developed in Ref. [33] which comprises two generalized lenses implemented by two spatial light modulators (SLMs) and a digital camera. The distance z between every two consecutive elements is fixed. Specifically, in the case of the coherenscope setup, these lenses L_j ($j = 1, 2$) have the following transmission functions

$$L_j(x,y) = \exp\left[-\frac{\mathrm{i}\pi}{\lambda \mathrm{g}_j}\left(x\cos\beta - y\sin\beta\right)^2\right]\exp\left[-\frac{\mathrm{i}\pi}{\lambda \mathrm{f}_\mathrm{j}}\left(x\sin\beta + y\cos\beta\right)^2\right], \tag{8}$$

where the focal lengths are $\mathrm{g}_1 = z$, $\mathrm{g}_2 = z/2$, and

$$\mathrm{f}_1 = 2z/\left(2 - \cot(\alpha/2)\right), \tag{9}$$

$$\mathrm{f}_2 = z/\left(2 - 2\sin\alpha\right), \tag{10}$$

are given as a function of the transformation angle $\alpha \in [\pi/2, 3\pi/2]$. These lenses yield the operation described by Eq. (7) except for a rotation at an angle $-\beta$ of the output beam. To compensate this effect and obtain the WD projection corresponding to the reported technique,

#188994 - $15.00 USD Received 17 Apr 2013; accepted 16 May 2013; published 22 May 2013

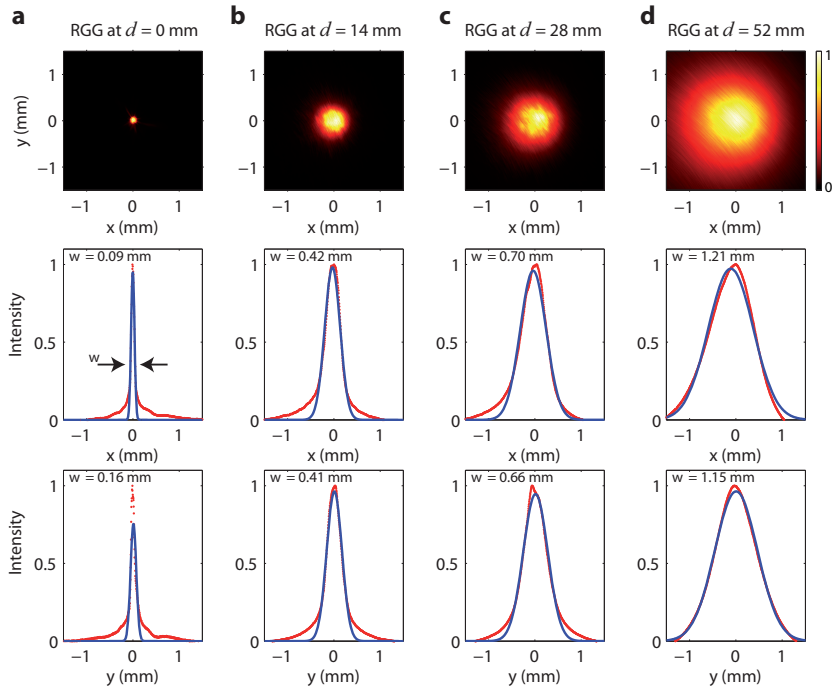

Fig. 6. Experimental results. (a-d), Intensity distributions of the the beam scattered from the RGG diffuser placed at different positions d. These signals were imaged just at the output plane of the diffuser. Their intensity profiles along the x and y directions are shown in the second and third row (red color, scatter plot), correspondingly. These profiles are fitted to a theoretical Gaussian curve (blue color, solid curve) to estimate the beam with w for each case.

the image acquired by the digital camera has to be rotated an angle β. This rotation can be digitally performed in real time using an image processing program as the one available in Matlab (e.g. *imrotate* using linear interpolation), or more advanced algorithms. Note that each lens is addressed into the SLM as the function $\arg[L_j(x,y)] \bmod 2\pi$. The SLMs simultaneously display the lenses $L_{1,2}$ because they are electronically controlled by the same device, which is connected to a personal computer via a DVI-port. Matlab programs for the setup automation and the data processing of the WD projections acquired by the CCD camera have been developed by us.

Generation partially coherent beams with Gaussian-envelope amplitude of degree of coherence

The generation of partially coherent beams with controlled degree of coherence is based on the Van Cittert-Zernike theorem [1, 2]. A Gaussian laser beam propagating through a rotating ground glass (RGG) diffuser emerges from it spatially incoherent with Gaussian intensity distribution $I(\mathbf{r}) = I_0 \exp\left(-2\pi \mathbf{r}^2/w^2\right)$, where I_0 is a normalization constant. The beam width w depends on the distance d between the diffuser and the back focal plane of the focusing lens, FL, (see Fig. 2(a), where the optical setup used for test beam generation is displayed). The larger the value of d, the larger value of w. The beam intensity distributions $I(\mathbf{r})$ on the output plane of the RGG diffuser for different distances, $d = 0$, 14, 28, and 52 mm, are shown in Fig. 6. Their measurements were performed by imaging the output plane of the diffuser into a CCD

camera using a $1\times$ telescope. The intensity profiles along x and y axes together with best-fitting Gaussian curves used for the beam width estimation are also displayed in the corresponding column Fig. 6 (a-d) .

According to the generalized Van Cittert-Zernike theorem, the MI of such a beam after its propagation through an optical system described by the point spread function (PSF) $h(\mathbf{r},\mathbf{r}')$, is given by

$$\Gamma_d\left(\mathbf{r}_1,\mathbf{r}_2\right) \propto \int \mathrm{d}\mathbf{r}' I(\mathbf{r}') h(\mathbf{r}_1,\mathbf{r}') h^*(\mathbf{r}_2,\mathbf{r}'). \tag{11}$$

The PSF of the system between the diffuser and the SLM, used for test signal generation [see Fig. 2(a)], is expressed as

$$h(\mathbf{r},\mathbf{r}') = \frac{1}{\mathrm{i}\lambda \mathrm{f}} \exp\left(\mathrm{i}\frac{\pi d}{\lambda \mathrm{f}^2}\mathbf{r}^2 - \mathrm{i}\frac{2\pi}{\lambda \mathrm{f}}\mathbf{r}'\cdot\mathbf{r}\right). \tag{12}$$

where $\mathrm{f} = 25\,\mathrm{cm}$ is the focal length of the collimating lens, CL. Using Eq. (11), the MI, $\Gamma_d\left(\mathbf{r}_1,\mathbf{r}_2\right)$, on the SLM plane is given by

$$\Gamma_d\left(\mathbf{r}_1,\mathbf{r}_2\right) = I_0 \exp\left[-\pi\frac{1}{w_c^2}\left(\mathbf{r}_1-\mathbf{r}_2\right)^2 + \mathrm{i}\pi\frac{1}{\rho^2}\left(\mathbf{r}_1^2-\mathbf{r}_2^2\right)\right]. \tag{13}$$

where $w_c = \sqrt{2}\lambda\mathrm{f}/w$ and $\rho = \mathrm{f}\sqrt{d/\lambda}$. Note that the MI as well as the degree of coherence, $\gamma_d\left(\mathbf{r}_1,\mathbf{r}_2\right) = \Gamma_d\left(\mathbf{r}_1,\mathbf{r}_2\right)/\sqrt{\Gamma_d\left(\mathbf{r}_1,\mathbf{r}_1\right)\Gamma_d\left(\mathbf{r}_2,\mathbf{r}_2\right)}$, have Gaussian amplitude and quadratic phase distribution. The parameter w_c, which can be considered as a radius of the coherence area, decreases when the distance d, and therefore w, increases.

We remind that, in order to shape the amplitude and phase of the beam, yielding a further modification of the MI, a phase hologram is addressed into the SLM [see Fig. 2(a)]. Moreover, since the plane of this SLM display is the conjugated one of the input plane of the coherenscope [SLM 1 display, see Fig. 2(b)], the MI of the studied beam is expressed as

$$\Gamma\left(\mathbf{r}_1,\mathbf{r}_2\right) = f(\mathbf{r}_1)\Gamma_d\left(\mathbf{r}_1,\mathbf{r}_2\right) f^*(\mathbf{r}_2) = \Gamma_c\left(\mathbf{r}_1,\mathbf{r}_2\right)\Gamma_d\left(\mathbf{r}_1,\mathbf{r}_2\right), \tag{14}$$

where $f(\mathbf{r})$ is the complex field amplitude of the beam encoded by the phase hologram. The amplitude of the coherence degree $|\gamma(\mathbf{r}_1,\mathbf{r}_2)|$ at the points where $f(\mathbf{r}) \neq 0$ equals $|\gamma_d\left(\mathbf{r}_1,\mathbf{r}_2\right)|$ and therefore it is also described by the same Gaussian profile. Notice, that $|\gamma_d\left(\mathbf{r}_1,\mathbf{r}_2\right)|$, and hence $|\gamma(\mathbf{r}_1,\mathbf{r}_2)|$, are homogeneous since they depend only on the distance $r = |\mathbf{r}_1 - \mathbf{r}_2|$.

Acknowledgements

The Spanish *Ministerio de Economía y Competitividad* is acknowledged for the project TEC2011-23629. A. Cámara thanks the financial support from the *Consejería de Educación de la Comunidad de Madrid* and the European Social Fund.